Anomalous Tensile Detwinning in Twinned Nanowires

Guangming Cheng, Sheng Yin, Tzu-Hsuan Chang, Gunther Richter, Huajian Gao, and Yong Zhu

Phys. Rev. Lett. **119**, 256101 — Published 21 December 2017

DOI: 10.1103/PhysRevLett.119.256101

Anomalous Tensile Detwinning in Twinned Nanowires

Guangming Cheng[1*], Sheng Yin[2*], Tzu-Hsuan Chang[1*], Gunther Richter[3], Huajian Gao[2#] and Yong Zhu[1#]

[1]Department of Mechanical and Aerospace Engineering, North Carolina State University, Raleigh, NC 27695, USA

[2]School of Engineering, Brown University, Providence, RI 02912, USA

[3]Max Planck Institute for Intelligent Systems, Heisenbergstrasse 3, D-70589 Stuttgart, Germany

[*]These authors contributed equally to this work.

#E-mail: huajian_gao@brown.edu; yong_zhu@ncsu.edu

Abstract

In spite of numerous studies on mechanical behaviors of nanowires (NWs) focusing on the surface effect, there is still a general lack of understanding on how internal microstructure of NWs influences their deformation mechanisms. Here, using quantitative *in situ* transmission electron microscopy (TEM) based nanomechanical testing and molecular dynamics (MD) simulations, we report a transition of deformation mechanism from localized dislocation slip to delocalized plasticity via an anomalous tensile detwinning mechanism in bi-twinned metallic NWs with a single twin boundary (TB) running parallel to the NW length. The anomalous tensile detwinning starts with detwinning of a segment of the preexisting TB under no resolved shear stress, followed by propagation of a pair of newly formed TB and grain boundary leading to large plastic deformation. An energy-based criterion is proposed to describe this transition of deformation mechanism, which depends on the volume ratio between the two twin variants and the cross-sectional aspect ratio.

Keywords:

Dislocation slip, Anomalous tensile detwinning, Large plasticity, Silver nanowire, *in situ* TEM

Metallic nanowires (NWs) are promising building blocks for a host of applications such as transparent electrodes, sensors, flexible/stretchable electronics, optoelectronics and nanoelectromechanical systems [1-4]. Operation and reliability of the NW-based devices call for a thorough understanding of their mechanical behaviors. Dislocation nucleation from free surfaces has been identified as a dominant deformation mechanism in NWs, in contrast to the forest dislocation dynamics in bulk materials. Extensive studies have been reported for defect-free, single crystalline metallic NWs where surface dislocation nucleation is dominant [5-16]. Such NWs exhibit ultrahigh yield strength [17,18], but typically with limited or no strain hardening and low tensile ductility due to the absence of effective obstacles within the NWs that could block the movement of dislocations. On the other hand, as-synthesized NWs typically possess different types of preexisting microstructures such as twin boundaries (TBs) [19-24], and there is still a general lack of understanding on how preexisting microstructures interact with the surface-nucleated dislocations and affect the mechanical behaviors of NWs.

TBs have been shown to be able to simultaneously increase the strength and ductility in bulk nanotwinned metals [25,26] and more recently in twinned metallic NWs [27-31]. Detwinning has been observed in nanotwinned metals, especially FCC metals [21,32-36], proposed mechanisms including cross-slip of partials at the TB [34] and migration of incoherent TBs formed by twinning partials [32,36]. In general the key to detwinning is to nucleate twinning partials by shear stress on a TB. Detwinning has also been observed recently in Cu nanopillars [21] and Au NWs [33] where preexisting TBs are inclined with respect to the loading directions. In all these cases, a finite resolved shear stress on a TB

is needed for detwinning. By contrast, in the present study, we report for the first time an anomalous detwinning mechanism involving no apparent resolved shear stress.

Here, based on a recently developed testing platform combining state-of-the-art microelectromechanical system (MEMS) technology, *in situ* TEM tensile tests and MD simulations, we conduct a systematic investigation of the deformation mechanisms in bi-twinned FCC metallic NWs, each having a single TB running parallel to the NW length direction. We identify two fundamental deformation mechanisms, localized dislocation slip and delocalized tensile detwinning. Transition of the two mechanisms depends on the volume ratio between the two twin variants and the cross-sectional aspect ratio, which can be explained by an energy-based criterion.

The Ag NWs in this study exhibit high crystalline quality owing to near-equilibrium growth conditions [17]. Figure 1(a) shows schematically the morphology of a ⟨110⟩ oriented bi-twinned NW with a single TB running parallel to the NW length direction. Cross-sectional TEM image of a typical bi-twinned NW is shown in Fig. 1(b), with a hexagonal cross-sectional shape but different arrangement of surface facets [marked in Fig. 1(a)] compared to its single crystalline counterpart [37]. High-resolution scanning TEM image in Fig. 1(d) shows that the internal TB in a bi-twinned NW is highly coherent without other line or planar defects typically seen in penta-twinned metallic NWs [28,29].

We performed *in situ* TEM tensile testing of individual NWs using a MEMS-based tensile testing stage (Fig. S4) that allows accurate measurements of both load and displacement simultaneously, as well as real-time imaging of microstructure evolution during deformation [38,39]. Figure 2 shows stress-strain responses and snapshots of

microstructure evolution of two typical bi-twinned Ag NWs under tensile tests. Insets in Figs. 2(a-b) show cross-sectional TEM images of the tested NWs, taken from the undeformed parts (beyond the clamps) after the tensile tests. The two bi-twinned NWs possess different volume ratios, defined as V_{small}/V_{large}, between the two twin variants [the insets in Figs. 2(a-b)], 0.56 and 0.19, respectively. The bi-twinned NW with a balanced (or large) volume ratio exhibited a limited fracture strain [3.5%, Figs. 2(a) and 2(c)], while the other with a small volume ratio showed large plasticity with an elongation of 34.5% [Figs. 2(b) and 2(d)], comparable to that of single crystalline NWs [37]. Moreover, the yield strength and the ultimate tensile strength (UTS) of the bi-twinned NWs, regardless of the deformation mode, were found to be 1.21-1.38 and 1.47-1.54 GPa (Fig. S5), respectively.

Localized dislocation nucleation and propagation is dominant in bi-twinned Ag NWs with balanced volume ratios [Fig. 2(c)]. Partial dislocations marked by blue arrow emerged upon yielding [Fig. 2(c)-*ii*]. After that, partial dislocations were continuously nucleated under increasing stress, leading to permanent planar sliding in the NW [Fig. 2(c)-*iii*] as they swiped across the whole cross section. Continuous dislocation nucleation and propagation resulted in the final failure of the NW [Figs. 2(c)-*iv*,*v* and Movie 1]. Note that only dislocation slip was observed without obvious necking at the fracture region [Fig. 3(a)]. According to the MD simulation results in Fig. 3(b-c) (Movie 3), a partial dislocation, i.e., $\alpha\boldsymbol{B}$ from plane ***BCD***, nucleated from a surface vertex [Fig. 3(b)-*i*], propagates in the dominant twin variant towards the preexisting TB (plane ***ABC***) [Fig. 3(b)-*ii*], interacts with the TB and then transmits into the small twin variant [Fig. 3(b)-*iii*], leaving behind a stair-rod dislocation $\alpha\alpha'$ with a magnitude of $\frac{2}{9}\langle 1\bar{1}1\rangle$ across the TB

(Fig. S11 and Tab. S1). After that, a trailing partial (***C*α** in plane ***BCD***) is nucleated [Fig. 3(b)-*iv*] and sweeps through the defected area, resulting in a permanent slipping step (one atomic layer along ***CB***) in the bi-twinned NW [Fig. 3(b)-*vi*]. Such localized dislocation slip led to failure of the NW with limited plastic strain, as shown in Fig. 3(a).

In contrast to the dislocation slip dominated deformation described above, large plasticity was observed in bi-twinned Ag NWs with small volume ratios [Figs. 2(b) and 2(d)], which was attributed to an anomalous tensile detwinning mechanism (Figs. S7, S8 and Movie 2). At the initial deformation stage, dislocations were nucleated and propagated in the dominant twin variant after yielding [Figs. 2(d)-*ii*,*iii*]; with further loading a permanent planar slip can also be observed [Fig. 2(d)-*iv*]. However, different from the localized dislocation slip, the dislocations in this case are nucleated and propagate in both ***BCD*** and ***ACD*** planes [Fig. 3(c)] and intersect at the preexisting TB. The interaction of multiple dislocations with the TB leads to detwinning of a segment of the TB, followed by the transition of ⟨110⟩ bi-twinned phase to ⟨001⟩ single crystalline phase [Fig. 2(d)-*v*] along the NW length, as evidenced by the cross-sectional TEM image and corresponding diffraction pattern in the insets in Fig. 4(k).

To further understand the tensile detwinning mechanism in bi-twinned metallic NWs, we have performed a series of MD simulations. We found that the mechanism includes two steps [Fig. 4(a)]. The first step is nucleation of a single crystalline embryo [Fig. 4(a)-*ii*] in the middle of the NW through multiple dislocation interactions on the original (preexisting) TB. In the second step [Fig. 4(a)-*iii*], further loading can lead to expansion of the single crystalline phase via continuous dislocation nucleation at the triple junction between the newly formed TB and grain boundary (GB) and the original TB. The

dislocation activities in the first step are illustrated in Figs. 4(b-e) (also see Fig. S12 and Movie 5). Generally, two partials, $\alpha\boldsymbol{B}$ and $\alpha\boldsymbol{C}$ nucleated from the free surface on the same slip plane [plane ***BCD*** in Fig. 3(c)] but neighboring atomic layers, react on the original TB and form a temporary partial $\boldsymbol{D}\alpha$, which decomposes into a stair-rod dislocation $\alpha\delta$ and a Hirth dislocation, $\frac{1}{3}\langle 010\rangle$ [40] [Fig. 4(b)]. Due to the high energy state of the two newly formed dislocations, an extended jog is formed among them with a new twinning partial $\boldsymbol{\delta C}$ in plane ***ABC*** (original TB) that will glide along $\langle 10\bar{1}\rangle$ or $\langle 011\rangle$ direction within the original TB [Fig. 4(c)]. When more dislocations react on the TB, as showed in Figure 4(d), partials $\boldsymbol{\alpha B}$ and $\boldsymbol{\alpha C}$ react with a partial $\boldsymbol{D\alpha}$ from the same twin variant but on the neighboring slip planes and two twinning partials $\boldsymbol{\delta C}$ and $\boldsymbol{\delta B}$ between them can be created. Figure 4(e) shows partials $\boldsymbol{\alpha' B}$ and $\boldsymbol{\alpha' C}$ in the mirror grain can also react with $\boldsymbol{D\alpha}$ on the neighboring slip planes and form two twinning partials $\boldsymbol{\delta C}$ and $\boldsymbol{\delta B}$ within the original TB. The newly nucleated partials from the free surface on neighboring slip planes will keep reacting on the original TB. Dislocation interactions as described in Fig. 4(b-e) keep contributing to the generation of twinning partials $\boldsymbol{\delta C}$ and $\boldsymbol{\delta B}$. These twinning partials span over several atomic planes, around 0.5 nm in length (dictated by the spacing of the reacting partials), whose glide within the original TB in $\langle 10\bar{1}\rangle$ or $\langle 011\rangle$ direction and induce detwinning of a small segment of the original TB, finally leading to the formation of a single crystalline embryo. At each end of the single crystalline embryo, where the single crystalline phase meets the bi-twinned phase, a unique TB-GB-TB structure is formed [Fig. 4(g)], which contains an inclined (new) TB in the dominant twin variant and a high-angle GB in the other twin variant. Once the

single crystalline embryo is formed, the step-two detwinning will dominate under further loading. Figure 4(i) shows continuous nucleation of twinning partials at the triple junction between the newly formed TB and GB and the original TB, leading to migration of the inclined TB and GB and expansion of the single crystalline phase (Movie 6). During the step-two detwinning, the bi-twinned NW with ⟨110⟩ axis is transformed into the single crystalline phase with ⟨001⟩ axis by TB and GB migration from the detwinning site [Figs. 4(f) and 4(h)]. Figures 4(j) and 4(k) show the fracture morphologies of the tensile detwinning dominated bi-twinned Ag NWs from MD simulations and experiments, respectively, which agreed very well.

In short, we found that a novel tensile detwinning deformation mechanism leads to the observed large plasticity in bi-twinned NWs with small volume ratios, characterized by interaction of multiple dislocations with the original TB. This mechanism is different from the dislocation slip dominated deformation in bi-twinned NWs with balanced volume ratios discussed earlier as well as the twinning dominated deformation in single crystalline NWs [37]. The two deformation mechanisms in bi-twinned NWs reported in the present study were observed in more tested samples (see additional examples in Fig. S6) and supported by MD simulations (Fig. S10 and Movies 3 and 4).

In the new tensile detwinning mechanism, whether the first step – nucleation of the single crystalline embryo – can occur determines the succeeding deformation mechanism. The energy change associated with the step-one detwinning process can be calculated as the energy needed to create the newly formed pair of TB and GB [Fig. 4(g)]:

$$\Delta E = 2A_1\gamma_{twin} + 2A_2\gamma_{GB} \quad (1)$$

where A_1 and A_2 are the areas of the TB and the high-angle GB in Fig. 4(f), respectively, γ_{twin} and γ_{GB} are the interfacial energies of TB and GB, respectively, with the values of 5.9 and 539 mJ/m^2 obtained from MD simulations. Eq. (1) describes the energy change of the system after the nucleation of the single crystalline embryo, in other words, it is the formation energy of the unique TB-GB-TB structure. Since in this step detwinning only occurs in an infinitesimal segment of the preexisting TB, the associated surface energy and TB energy change is neglected in Eq. (1). Figure 5(a) plots this energy change as a function of the volume ratio for a NW with fixed H = 9 nm and W = 13 nm. The volume ratio in bi-twinned NWs can be quite different, ranging from 0.1 to 1.0 in the 19 NWs examined in our experiments. It can be seen that ΔE can be reduced by decreasing the volume ratio, indicating that a reduced volume ratio can facilitate the detwinning process in bi-twinned NWs.

To systematically investigate the transition of the two deformation mechanisms in bi-twinned NWs, a parametric study was conducted in MD simulations. The inset in Fig. 5(a) shows the cross-section of the simulated bi-twinned NWs, where W, H and h_1 are the independent geometric parameters considering the fixed angles of the facets [Fig. 1(a)]. For a given value of H, the energy change of the detwinning process ΔE in Eq. (1) can be expressed in terms of two dimensionless parameters: H/W and volume ratio $r \in (0,1]$ (see Supplementary Information Section S6):

$$\Delta E(A_1, A_2) = \Delta E(W, H, h_1) = \Delta E(H, H/W, r) \tag{2}$$

The contour of ΔE is plotted in Fig. 5(b) for a fixed H = 8.9 nm, where the x-axis is H/W and the y-axis is r. The color from blue to red indicates an increase in ΔE. The value

of ΔE varies for different H, but the contour lines are the same regardless of H. The plot shows that NWs with smaller volume ratio and larger *H/W* have lower energy change, thus favoring tensile detwinning; while those with larger volume ratio and smaller *H/W* have higher energy change, thus favoring localized dislocation slip. In addition to the localized dislocation slip and tensile detwinning, a transitional mode (Fig. S14) can be identified in MD simulations. In this mode, dislocation slip dominates initially, leading to necking of the NW in the *W* direction, which increases the *H*/*W* value in the necked region. This geometrical change thus makes detwinning more favorable in the necked region.

Based on the experimental and simulation results, a transition line, corresponding to a critical ΔE of 140eV for H=8.9nm, was found to reasonably separate the localized dislocation slip and the tensile detwinning mechanisms in bi-twinned Ag NWs [Fig. 5(b)]. Our simulation results over 100 different case studies showed good agreement with the prediction based on ΔE. The transitional mode of mixed deformation mechanisms was frequently seen around this transition line. In addition, a total of 19 experimental data are included in Fig. 5(b), also in good agreement with the prediction based on ΔE.

In conclusion, we have discovered a transition between two deformation mechanisms, localized dislocation slip and delocalized tensile detwinning, in bi-twinned Ag NWs. Localized dislocation nucleation and propagation across the TB led to limited plasticity in bi-twinned NWs with balanced volume ratios, while delocalized tensile detwinning deformation resulted in large plasticity in those with small volume ratios. The detwinning process was unexpected in view of no apparent resolved shear stress on the preexisting TB, which was attributed to the novel tensile detwinning mechanism – nucleation of a

single crystalline embryo as a result of multiple dislocation interactions on the preexisting TB (step-one), followed by migration of the unique TB-GB-TB structure (step-two). Our experimental and theoretical results indicated that the deformation mode of a bi-twinned NW is governed by the step-one detwinning. An energy-based criterion for the anomalous tensile detwinning was proposed, which was able to capture the effects of the volume ratio and cross-sectional aspect ratio on the transition of deformation mechanisms in bi-twinned NWs.

Acknowledgements

The authors acknowledge financial support from the National Science Foundation (NSF) under Award Nos. DMR-1410475 and DMR-1709318. The authors acknowledge the use of the Analytical Instrumentation Facility (AIF) at North Carolina State University, which is supported by the State of North Carolina and NSF (Award No. ECCS-1542015), and computational support by the Extreme Science and Engineering Discovery Environment (XSEDE) through Grant MS090046.

References

[1] J.-Y. Lee, S. T. Connor, Y. Cui, and P. Peumans, Nano letters **8**, 689 (2008).
[2] A. Tao, F. Kim, C. Hess, J. Goldberger, R. He, Y. Sun, Y. Xia, and P. Yang, Nano Letters **3**, 1229 (2003).
[3] F. Xu and Y. Zhu, Advanced materials **24**, 5117 (2012).
[4] M. Li, R. B. Bhiladvala, T. J. Morrow, J. A. Sioss, K.-K. Lew, J. M. Redwing, C. D. Keating, and T. S. Mayer, Nature Nanotechnology **3**, 88 (2008).
[5] J. R. Greer and J. T. M. De Hosson, Progress in Materials Science **56**, 654 (2011).
[6] T. Zhu and J. Li, Progress in Materials Science **55**, 710 (2010).
[7] C. R. Weinberger and W. Cai, Journal of Materials Chemistry **22**, 3277 (2012).
[8] H. S. Park, K. Gall, and J. A. Zimmerman, Physical Review Letters **95**, 255504 (2005).
[9] T. Zhu, J. Li, A. Samanta, A. Leach, and K. Gall, Physical Review Letters **100**, 025502 (2008).
[10] H. Zheng, A. Cao, C. R. Weinberger, J. Y. Huang, K. Du, J. Wang, Y. Ma, Y. Xia, and S. X. Mao, Nature communications **1**, 144 (2010).
[11] Y. Yue, P. Liu, Q. Deng, E. Ma, Z. Zhang, and X. Han, Nano letters **12**, 4045 (2012).
[12] L. Y. Chen, M.-r. He, J. Shin, G. Richter, and D. S. Gianola, Nature Materials **14**, 707 (2015).
[13] B. Roos, B. Kapelle, G. Richter, and C. Volkert, Applied Physics Letters **105**, 201908 (2014).
[14] C. R. Weinberger, A. T. Jennings, K. Kang, and J. R. Greer, Journal of the Mechanics and Physics of Solids **60**, 84 (2012).
[15] Y. Zhu, Applied Mechanics Reviews **69**, 010802 (2017).
[16] W. Liang and M. Zhou, Journal of Engineering Materials and Technology **127**, 423 (2005).
[17] G. Richter, K. Hillerich, D. S. Gianola, R. Moenig, O. Kraft, and C. A. Volkert, Nano Letters **9**, 3048 (2009).
[18] B. Wu, A. Heidelberg, and J. J. Boland, Nature Materials **4**, 525 (2005).
[19] Y. Lu, J. Song, J. Y. Huang, and J. Lou, Advanced Functional Materials **21**, 3982 (2011).
[20] C. Deng and F. Sansoz, Acta Materialia **57**, 6090 (2009).
[21] D. Jang, X. Li, H. Gao, and J. R. Greer, Nature Nanotechnology **7**, 594 (2012).
[22] R. A. Bernal, A. Aghaei, S. Lee, S. Ryu, K. Sohn, J. Huang, W. Cai, and H. Espinosa, Nano Letters **15**, 139 (2015).
[23] T. Filleter *et al.*, Small **8**, 2986 (2012).
[24] Y. Zhu, Q. Qin, F. Xu, F. Fan, Y. Ding, T. Zhang, B. J. Wiley, and Z. L. Wang, Physical Review B **85**, 045443, 045443 (2012).
[25] X. Li, Y. Wei, L. Lu, K. Lu, and H. Gao, Nature **464**, 877 (2010).
[26] K. Lu, L. Lu, and S. Suresh, Science **324**, 349 (2009).
[27] J. Wang, F. Sansoz, J. Huang, Y. Liu, S. Sun, Z. Zhang, and S. X. Mao, Nature communications **4**, 1742 (2013).
[28] S. Narayanan, G. Cheng, Z. Zeng, Y. Zhu, and T. Zhu, Nano letters **15**, 4037 (2015).

[29] Q. Qin, S. Yin, G. Cheng, X. Li, T.-H. Chang, G. Richter, Y. Zhu, and H. Gao, Nature communications **6**, 5983 (2015).
[30] F. Niekiel, E. Spiecker, and E. Bitzek, Journal of the Mechanics and Physics of Solids **84**, 358 (2015).
[31] J. Wang and H. Huang, Applied Physics Letters **88**, 203112 (2006).
[32] J. Wang, N. Li, O. Anderoglu, X. Zhang, A. Misra, J. Y. Huang, and J. P. Hirth, Acta Materialia **58**, 2262 (2010).
[33] S. Lee, J. Im, Y. Yoo, E. Bitzek, D. Kiener, G. Richter, B. Kim, and S. H. Oh, Nature communications **5**, 3033 (2014).
[34] Y. T. Zhu, X. L. Wu, X. Z. Liao, J. Narayan, L. J. Kecskés, and S. N. Mathaudhu, Acta Materialia **59**, 812 (2011).
[35] H. Zhou, X. Li, Y. Wang, Z. Liu, W. Yang, and H. Gao, Nano letters **15**, 6082 (2015).
[36] Y. M. Wang, F. Sansoz, T. LaGrange, R. T. Ott, J. Marian, T. W. Barbee Jr, and A. V. Hamza, Nature Materials **12**, 697 (2013).
[37] J.-H. Seo *et al.*, Nano Letters **11**, 3499 (2011).
[38] T.-H. Chang, G. Cheng, C. Li, and Y. Zhu, Extreme Mechanics Letters (2016).
[39] T.-H. Chang and Y. Zhu, Applied Physics Letters **103**, 263114 (2013).
[40] J. P. Hirth and J. Lothe, *Theory of dislocations* (John Wiley & Sons, New York, 1982), 2 nd edn.
[41] See Supplemental Material for Methods, which includes Refs.[42-45]
[42] S. Plimpton, J Comput Phys **117**, 1 (1995).
[43] P. L. Williams, Y. Mishin, and J. C. Hamilton, Modelling and Simulation in Materials Science and Engineering **14**, 817 (2006).
[44] S. Nose, J Chem Phys **81**, 511 (1984).
[45] A. Stukowski, Modelling and Simulation in Materials Science and Engineering **18**, 015012 (2010).

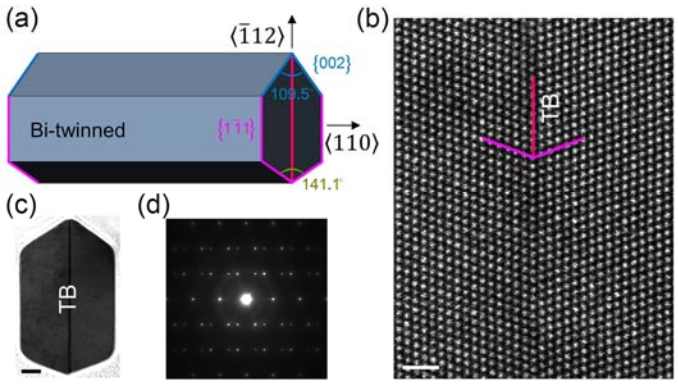

FIG. 1. (a) Schematic drawing of a bi-twinned NW. (b,c) Cross-sectional TEM image and corresponding diffraction pattern of a bi-twinned Ag NW, respectively. Scale bar, 20 nm. (d) A cross-sectional high-resolution STEM image of a bi-twinned Ag NW. Scale bar, 1 nm.

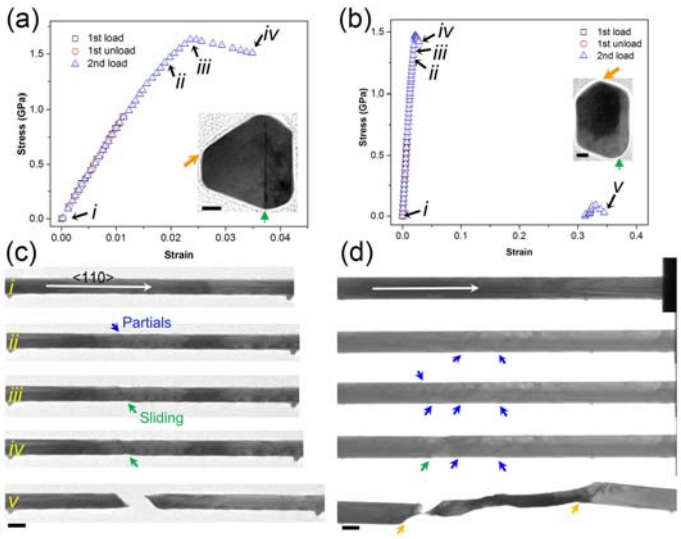

FIG. 2. (a,b) Engineering stress-strain curves of bi-twinned Ag NWs with balanced and small volume ratio, respectively. Insets in (a,b) are the corresponding cross-sectional images of the tested NWs (each sectioned from the undeformed part after the test). Location of the TB is marked by a green arrow. Scale bar, 20 nm. (c,d) Snapshots of microstructure evolutions corresponding to (a,b), respectively. The five snapshots in each case correspond to the data points marked in (a,b). Partial dislocations are marked by blue arrows and planar sliding by green arrows. The viewing directions are from the $\langle 1\bar{1}0 \rangle$ zone axis of the large twin variant in (c,d), which are marked by the orange arrows in the insets in (a,b). The new inclined TBs in (d) are marked by orange arrows. Scale bar, 100 nm.

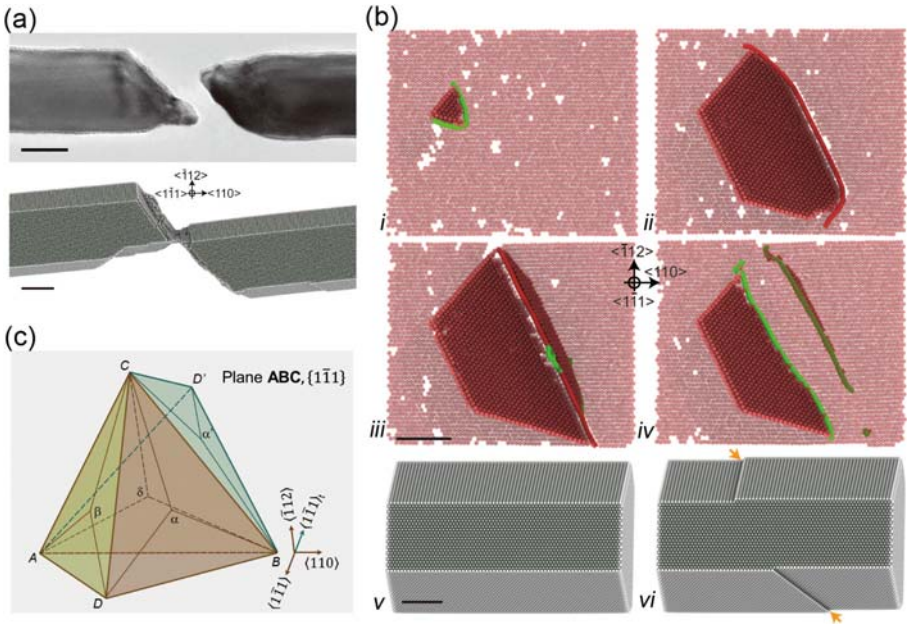

FIG. 3. (a) Fracture morphologies of the bi-twinned Ag NWs with balanced volume ratios from experiments and simulations, respectively. Scale bar, 100 nm for experiments and 5 nm for simulations. (b) Snapshots from MD simulations showing nucleation, propagation of partial dislocations and interaction between the partials and the TB. A permanent slip step with one atomic layer is marked by an orange arrow in (b-vi). Scale bar, 2.5 nm. (c) Illustration of a double Thompson tetrahedron on the coherent $\{1\bar{1}1\}$ TB in bi-twinned NWs. The front tetrahedron (***ABCD***) represents the matrix slip systems in the dominant twin variant, while the back one (***ABCD'***) represents twin slip systems in the small twin variant.

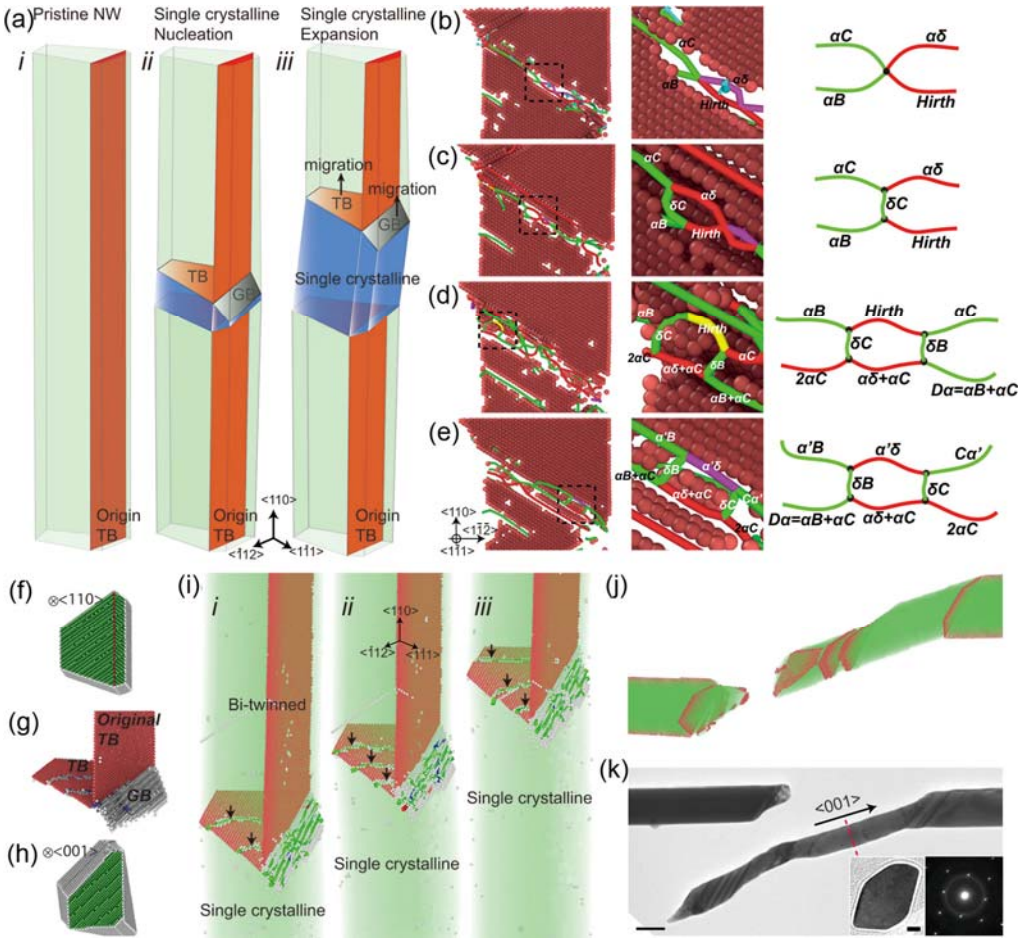

FIG. 4. (a) Schematics showing two steps of the tensile detwinning mechanism. *i*, The pristine bi-twinned NW; *ii*, Step-one detwinning showing the formation of a single crystalline embryo (colored by blue) with a unique TB-GB-TB structure; *iii*, Step-two detwinning showing the expansion of the single crystalline phase. (b-e) Representative dislocation reactions during step-one detwinning process. Only hexagonal close-packed atoms are made visible. (f,h) Cross-section of the bi-twinned phase with axial direction of ⟨110⟩ and the single crystalline phase with the axial direction reoriented to ⟨001⟩, respectively. (g) Detailed structure of the newly formed TB-GB-TB structure during step-one detwinning process. (i) MD snapshots in step-two detwinning showing migration of the newly formed inclined TB and GB. Black arrows indicate the partials on the inclined

TB that are responsible for the TB migration. (j,k) Fracture morphology of the bi-twinned Ag NWs with small volume ratios from experiments and simulations, respectively. The insets in (k) show the cross-sectional TEM image and corresponding diffraction pattern (zone axis, ⟨001⟩) from the single crystalline phase in the deformed part. Scale bar in (k) and in the inset, 100 and 20 nm, respectively.

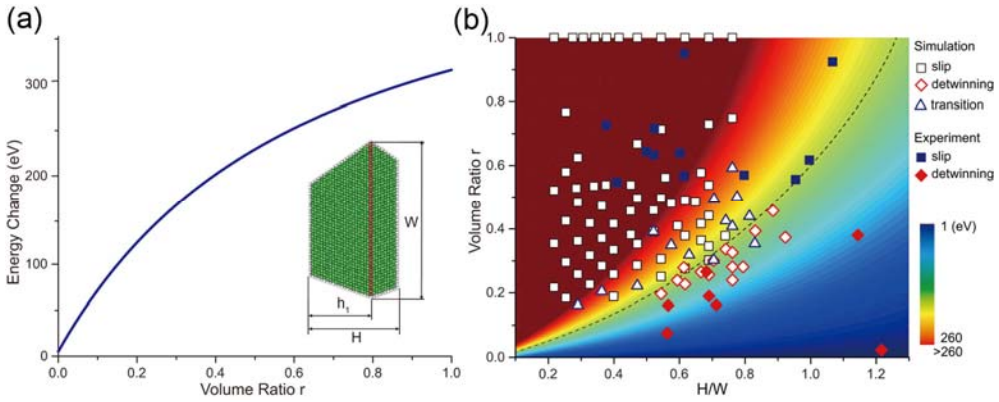

FIG. 5. (a) Energy change associated with the detwinning process as a function of the twin volume ratio for a sample with fixed W and H. Inset in (a) shows the cross section of a typical bi-twinned NW in MD simulations and its corresponding geometric parameters. (b) Contour plot of energy change in the detwinning process for a fixed H as a function of *H/W* and twin volume ratio r, along with simulation and experimental data. For the simulation results, open black squares, open red rhombuses and open blue triangles stand for the slip dominated mode, the tensile detwinning mode and the transitional deformation mode, respectively. For the experiment results, solid blue squares and solid red rhombuses stand for the slip dominated mode and the tensile detwinning mode, respectively.